Dual-band Complementary Compensation for a 2-Coil Single-ended IPT Converter Achieving Omnidirectional Misalignment Tolerance across a Wide Load Range

Jingyu Wang, *Student Member, IEEE* and Zhicong Huang, *Senior Member, IEEE*

***Abstract*—Misalignment tolerance is essential for robust inductive power transfer (IPT). For the passive approaches, achieving improved omnidirectional misalignment tolerance across a wide load range remains challenging. This paper presents a dual-band complementary compensation design for a 2-coil single-ended IPT converter to achieve enhanced omnidirectional misalignment tolerance under wide load variations and arbitrary magnetic coupler parameters. By exploiting the high second harmonic content in a single-ended IPT inverter, the proposed approach establishes different power transfer channels for fundamental and second harmonic components, specifically designed with proportional and inverse proportional relationships to mutual inductance, respectively. The proposed method achieves power fluctuation mitigation under misalignment conditions by using the second harmonic. The notable advantage of this method is that it realizes omnidirectional misalignment tolerance across a wide load range, which reduces the design requirements for the magnetic coupler and control circuits compared to other approaches. This paper conducts modeling and analysis of harmonics in single-ended IPT circuits, followed by compensation design and parameter optimization for misalignment tolerance enhancement. Experimental verification proves the validity of the theoretical framework.**

***Index Terms*—Omnidirectional Misalignment tolerance, Load-independent output, Inductive power transfer, Second harmonic, Single-ended.**

I. Introduction

INDUCTIVE power transfer (IPT) stands out as an exceptional method for power transfer, offering the advantages of being contactless, safe, and convenient [1], [2]. Its versatility spans a wide range of applications and power levels, including consumer electronics [3]–[5], biomedical implants [6], [7], and electric vehicles [8]–[10]. Despite its many advantages, misalignment between the transmitter (Tx) and receiver (Rx) pads remains a significant issue that negatively impacts power transfer efficiency and overall system performance. Therefore, improving omnidirectional tolerance to misalignment is crucial for the design and implementation of IPT systems.

Regarding the enhancement of misalignment tolerance in IPT circuits, existing research typically includes both active and passive approaches. The active approach involves the modulation control-based methods, while the passive approaches include magnetic coupler-based, compensation network-based, and dual-frequency-based methods.

For the modulation control-based method, the pulse width modulation (PWM) is a common method. However, the PWM modulation is generally constrained by duty cycle limitations, only capable of addressing power fluctuations within narrow ranges [11], [12]. Although pulse frequency modulation (PFM) enables power regulation across wider ranges, it induces system detuning that degrades operational efficiency [13], [14]. Additionally, pulse density modulation (PDM) includes burst firing control [26] and ON-OFF keying modulation [27], all of which are effective. These techniques will produce non-negligible subharmonics. In addition, the above methods require a significant number of switching devices, along with corresponding drive, detection, and control circuits.

To avoid the complex detection and control circuits and to improve the robustness of IPT systems, more research is focused on the passive approaches as follows:

For the magnetic coupler-based method, this kind of method enhances magnetic field coupling under misalignment conditions through the incorporation of auxiliary coils. A rectangular-solenoidal pad (RSP) composed of a rectangular pad and a solenoid pad at the transmitting or receiving sides is studied in [16], [17]. This approach leverages the principle of magnetic flux complementarity between the unipolar rectangular coil and the bipolar solenoid coil when the coils are misaligned, ensuring stable magnetic flux during misalignment. However, this method is limited to improving tolerance for misalignment in only one direction. Building on this, a quadrupolar or an orthogonal solenoid coil is used in place of the single solenoid to enhance misalignment tolerance in both the X and Y directions [18], [19]. Nonetheless, the proposed solution does not address situations where misalignment occurs simultaneously in the Z, X, and

Manuscript submitted May 12, 2025, revised September 15, 2025, accepted October 23, 2025. This work was supported by the National Natural Science Foundation of China under Grant 52577198, the Guangzhou Municipal Science and Technology Bureau under Grant 2025A04J7064, and the Fundamental Research Funds for the Central Universities under Grant 2025ZYGXZR041. (Corresponding author: Zhicong Huang)

J. Wang and Z. Huang are with the Shien-Ming Wu School of Intelligent Engineering, South China University of Technology, Guangzhou, 510006, China (e-mail: zhiconghuang@scut.edu.cn).

TABLE I
A COMPARISON OF DUAL-FREQUENCY METHODS FOR MISALIGNMENT TOLERANCE

References	Topplogy	Switch Number	Coil Number	Resonant or detuning	Load-independent output	The ratio of harmonics	Design flexibility of misalignment tolerance	Load range	Shoot-through Issue
[28]	Full-bridge	4	2	Detuning	No	3rd/1st=33.3%	High	fixed load	Yes
[29]	Full-bridge	4	2	Resonant	No	3rd/1st=33.3%	Low	fixed load	Yes
[30]	Full-bridge	4	6	Resonant	Yes	3rd/1st=32.57%	Low	Wide	Yes
Proposed	Single-ended	1	2	Resonant	Yes	2ed/1st=68.5%	High	Wide	No

Y directions. In summary, the magnetic coupler-based method imposes stringent design requirements on magnetic couplers, necessitating the implementation of two or more magnetic coupler channels. Furthermore, this method cannot realize omnidirectional misalignment tolerance enhancement.

For the compensation network-based method, the hybrid IPT circuit constitutes a methodology implemented through a compensation network and a simple coil configuration design to improve the misalignment tolerance. A hybrid coil structure and corresponding compensation design method were proposed in [20], which utilizes decoupling between rectangular and double-D coils to create power transfer channels that are both directly and inversely proportional to mutual inductance. This study also introduces a series of compensation network design techniques. However, it is only effective for improving misalignment tolerance in the X and Z directions. When coil misalignment occurs in the Y direction, the decoupling between coils is disrupted, leading to reactive current circulation in the circuit system. To address this issue, an orthogonal double-D hybrid coil structure was proposed in [21], [22], which improves the misalignment tolerance for single horizontal and Z-direction. However, when misalignment occurs simultaneously in the X and Y directions, the above problems will still occur. Furthermore, this method still relies on multi-channel magnetic couplers and cannot achieve omnidirectional misalignment tolerance enhancement. The detuned design methodology is also recognized as a compensation network-based method, which employs a simple magnetic coupler configuration by designing the operating frequency within a misalignment-insensitive region to enhance tolerance [23], [24]. However, this approach compromises the circuit's power transfer capability and efficiency.

The above passive approaches fail to achieve omnidirectional misalignment tolerance with a single 2-coil magnetic coupler.

For the dual-frequency-based methods summarized in Table I, a dual-frequency detuning approach was proposed in [28] to achieve omnidirectional misalignment tolerance using a single 2-coil magnetic coupler. However, this method degrades both power transfer capability and efficiency and is only applicable under fixed load conditions. To improve these performances, a dual-frequency tuning strategy was introduced in [29]. Nevertheless, this technique can only adjust misalignment tolerance by redesigning coil parameters, leading to constrained flexibility, and remains limited to fixed-load applications. A multi-coil dual-frequency WPT circuit was presented in [30], but its coil structure is complex and prone to cross-coupling effects. Additionally, all aforementioned dual-frequency methods utilize the fundamental and third harmonic components. Since the third harmonic voltage amplitude in the input AC supply is relatively low (only one-third of the fundamental), achieving effective power transfer necessitates large harmonic currents.

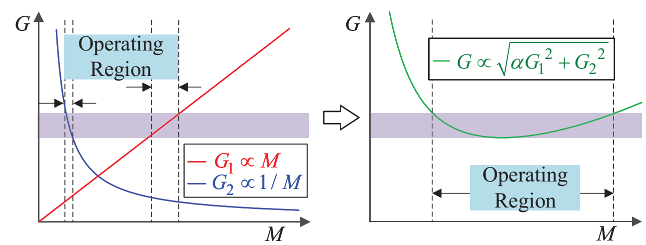

Fig. 1. Operating principle.

For the passive approaches, achieving improved omnidirectional misalignment tolerance across a wide load range remains challenging. This paper presents a dual-band complementary compensation design for a 2-coil single-ended IPT converter, achieving enhanced omnidirectional misalignment tolerance across a wide load range and with arbitrary magnetic coupler parameters, which reduces the design requirements for the magnetic coupler and control circuits. The single-ended IPT converter adopted in this paper has been revealed to have a significant second harmonic component that could be used for power transfer, whereas prior to this, the second harmonic component was typically ignored [31]. Therefore, the proposed method establishes power transfer channels for the second harmonic generated by the inverter, while simultaneously utilizing them to counteract power fluctuations caused by misalignment conditions. The fundamental operating principle is illustrated in Fig. 1. The notable advantage of this method is that it realizes omnidirectional misalignment tolerance across a wide load range. In addition, the proposed method can be effective with arbitrary 2-coil magnetic coupler parameters. The key contributions of this paper are highlighted as follows:

1) This paper first reports the use of the significant second harmonic component for omnidirectional misalignment tolerance improvement in a single-switch IPT circuit (fewer power switches, significant second harmonic, and avoiding the shoot-through issue).
2) This paper proposes a dual-band complementary compensation for a 2-coil single-ended IPT converter, achieving omnidirectional misalignment tolerance across a wide load range and load-independent output.
3) Compared with other dual-frequency resonant methods, the proposed method is independent of the design of the

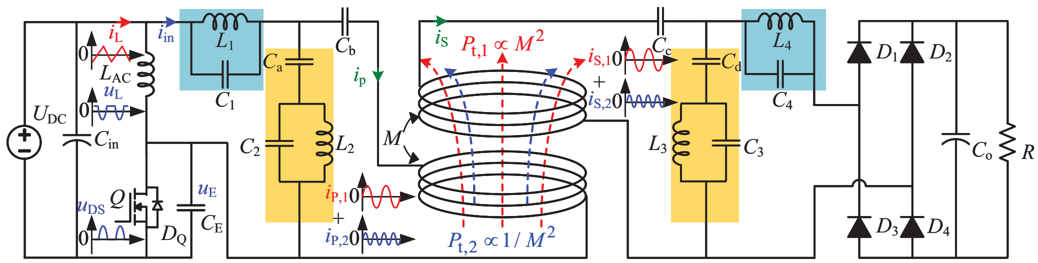

Fig. 2. Proposed circuit.

magnetic coupler and exhibits universal applicability to 2-coil magnetic couplers with arbitrary parameters.

This paper first introduces the schematic of the proposed system. It then models the output voltage of the single-ended IPT inverter and highlights the significant presence of second harmonic components in the output voltage. This paper subsequently provides a detailed analysis of the transfer channels and equivalent circuits for both the fundamental and second harmonics in the proposed circuit. Building on this, the paper further examines the parameter configuration method to enhance the misalignment tolerance of the circuit and investigates its overall characteristics. Finally, this paper verifies the effectiveness of the proposed method through simulation and experimental validation.

II. Proposed Circuit Topology and Operating Principle

A. Schematic of the Proposed System

This paper proposes a dual-band complementary compensation for a 2-coil single-ended IPT converter achieving omnidirectional misalignment tolerance, whose schematic representation appears in Fig. 2. The proposed configuration employs a single-ended inverter topology to generate precisely regulated high-frequency AC power [32], [33]. The load-independent characteristic guarantees that the inverter's voltage waveform (u_{L}) maintains stability under varying load conditions, thereby ensuring stable harmonic components. Fig. 2 further demonstrates the operational waveforms of the AC inductor L_{AC}. The $P_{\mathrm{t},1}$ and $P_{\mathrm{t},2}$ represent the power transfer in coils of fundamental and second harmonic, respectively.

B. High-order Harmonic Issue

The operational waveforms of the proposed IPT driver are characterized during one operational cycle in Fig. 3. Notably, the voltage waveform $u_{\mathrm{L}}(t)$ exhibits two operational modes: *DC clamped mode* and *underdamped mode*. To quantitatively evaluate the harmonics content in u_{L}, we implement a hierarchical waveform simplification methodology comprising two sequential analytical stages.

1) The voltage waveform u_{L} during underdamped resonant operation can be mathematically represented as a truncated sinusoidal segment, as experimentally validated in Fig. 3(a). Consequently, the analytical expression for u_{L} admits a piecewise-defined formulation:

$$u_{\mathrm{L}}(t)=\begin{cases}-A\sin(\omega_0 t+\varphi), & 0\le t<t_1\\ U_{\mathrm{DC}}, & t_1\le t\le T\end{cases} \tag{1}$$

where A, ω_0, and φ respectively denote the sinusoidal waveform's peak amplitude, angular frequency, and initial phase angle. Given the periodic nature of u_{L}, the boundary condition $u_{\mathrm{L}}(0)=U_{\mathrm{DC}}$ is derived through Volt-Second balance analysis.

2) During transient intervals (0, t_{a}) and (t_{b}, t_1), the voltage waveform u_{L} admits piecewise linear approximations, enabling regions ① and ② to be modeled as triangular profiles. These temporally symmetric intervals share an identical duration Δt, defined mathematically as:

$$\Delta t=t_a-0=t_1-t_b=\frac{\pi\arcsin(\frac{U_{\mathrm{DC}}}{A})}{180\mathrm{deg}\omega_0}. \tag{2}$$

Fig. 3(b) demonstrates that regions ① and ② can be consolidated into a unified rectangular profile labeled ①+② through waveform reconstruction. This synthesis enables u_{L} to be transformed into a simplified piecewise-continuous waveform, expressed as:

$$u_{\mathrm{L}}(t)=\begin{cases}0, & 0\le t<t_{\mathrm{a}}\\ -A\sin[\omega_0(t-t_{\mathrm{a}})], & t_{\mathrm{a}}\le t<t_{\mathrm{b}}\\ U_{\mathrm{DC}}. & t_{\mathrm{b}}\le t\le T\end{cases} \tag{3}$$

To obtain the amplitude of arbitrary harmonics of $u_{\mathrm{L}}(t)$, ω_0 and A should be calculated first.

According to the above analysis, ω_0 could be expressed by

$$\omega_0=\frac{\pi}{t_{\mathrm{b}}-t_{\mathrm{a}}}=\frac{\pi}{(1-D-D_{\mathrm{Z}})T-2\Delta t}, \tag{4}$$

where D is the duty cycle of switch Q and D_{Z} is the ZVS margin of the switch.

When calculating A, the principle of voltage-second balance on $L_{\mathrm{P},1}$ within a cycle should be applied:

$$U_{\mathrm{DC}}(T-t_{\mathrm{b}})=\int_{t_{\mathrm{a}}}^{t_{\mathrm{b}}}A\sin[\omega_0(t-t_{\mathrm{a}})]\mathrm{d}t=\frac{2A}{\pi}(t_{\mathrm{b}}-t_{\mathrm{a}}). \tag{5}$$

With (3), (4) and (5), A can be derived as

$$A=\frac{\pi U_{\mathrm{DC}}\left[(D+D_{\mathrm{Z}})T+\Delta t\right]}{2\left[(1-D-D_{\mathrm{Z}})T-2\Delta t\right]}. \tag{6}$$

$$a_{\mathrm{n}} = \frac{2}{T}\int_{t_{\mathrm{a}}}^{t_{\mathrm{b}}} (-A)\sin(\omega_0 t)\sin(\mathrm{n}\omega_{\mathrm{s},1}\mathrm{t})\mathrm{dt} + \frac{2}{T}\int_{t_{\mathrm{b}}}^{T} U_{\mathrm{DC}}\sin(\mathrm{n}\omega_{\mathrm{s},1}\mathrm{t})\mathrm{dt}, \tag{8a}$$

$$b_{\mathrm{n}} = \frac{2}{T}\int_{t_{\mathrm{a}}}^{t_{\mathrm{b}}} (-A)\sin(\omega_0 t)\cos(\mathrm{n}\omega_{\mathrm{s},1}\mathrm{t})\mathrm{dt} + \frac{2}{T}\int_{t_{\mathrm{b}}}^{T} U_{\mathrm{DC}}\cos(\mathrm{n}\omega_{\mathrm{s},1}\mathrm{t})\mathrm{dt}. \tag{8b}$$

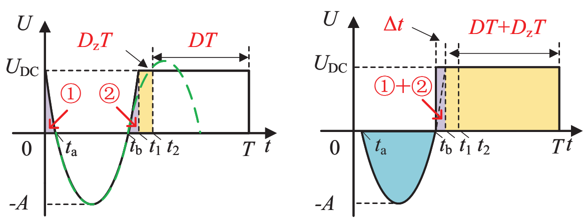

(a) Sinusoidal approximation (b) Wave re-shaping

Fig. 3. Simplification of the waveform of $u_{\mathrm{L}}(t)$ for calculation.

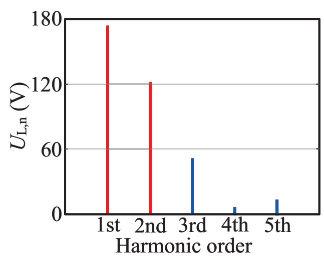

Fig. 4. Calculated harmonic components of u_{L}.

After obtaining both ω_0 and A, the curve in Fig. 3(b) can be decomposed into its Fourier components, as given by (7).

$$u_{\mathrm{L}}(t) = \sum_{\mathrm{n}=1}^{\infty} [a_{\mathrm{n}}\cos(\mathrm{n}\omega_{\mathrm{s},1}\mathrm{t}) + \mathrm{b}_{\mathrm{n}}\sin(\mathrm{n}\omega_{\mathrm{s},1}\mathrm{t})], \tag{7}$$

where a_{n} and b_{n} are calculated by equations (8a) and (8b), respectively. And $\omega_{\mathrm{s},1}$ is the operating angle frequency.

Therefore, the amplitude of arbitrary harmonics of u_{L} can be expressed as

$$U_{\mathrm{L,n}} = \sqrt{a_{\mathrm{n}}^2 + b_{\mathrm{n}}^2}. \tag{9}$$

For example, a single-ended IPT converter with circuit parameters given in Table II is considered. Based on (9), the harmonic components of u_{L} can be calculated and plotted in Fig. 4. To discern the parameters associated with these harmonics, the subscript “1” will represent the fundamental component, while the subscript “2” signifies the second-order harmonic. By referring to Fig. 4, the second harmonic holds notable importance and a relationship between the fundamental and second components of u_{L} as $U_{\mathrm{L},2} \approx 0.685U_{\mathrm{L},1}$ can be established for the subsequent analysis and design in this paper.

TABLE II
PARAMETER DESIGN OF THE SINGLE-ENDED IPT DRIVER

Parameter	Definition	Value
f_{s}	Operating frequency	100 kHz
U_{DC}	Input DC voltage	100 V
D	Duty cycle	0.5
D_{Z}	ZVS margin	0.11

III. LOAD-INDEPENDENT OUTPUT AND ANALYSIS OF MISALIGNMENT TOLERANCE

A. Analysis of Load-Independent Output

It has been widely studied that the characteristics of the S-S and LCC-LCC compensation at resonant frequency are summarized in Table III. To achieve the operational features depicted in Fig. 1 and realize load-independent constant-current (CC) output capability, this paper aims to configure the S-S and LCC-LCC as a dual-band complementary compensation.

Fig. 5 elucidates the configuration methodology of the proposed compensation network. When operating at $\omega_{\mathrm{s},1}$ (Fundamental-harmonic angular frequency) in Fig. 5(b), the blue-shaded network section is equivalently represented as an inductor while the yellow-shaded section functions as a capacitor, thereby establishing an overall LCC-LCC compensation topology. However, under $\omega_{\mathrm{s},2}$ (Second-harmonic angular frequency) operation in Fig. 5(c), the blue-shaded network manifests capacitive characteristics while the transparent network portions behave as open circuits, consequently realizing an S-S compensation topology configuration.

To achieve simultaneous resonance of both fundamental and second harmonic components, this work establishes the inductive-capacitive resonance relationship within the circuit topology depicted in Fig. 5 as follows:

TABLE III
S-S AND LCC-LCC TOPOLOGIES FOR IPT SYSTEM AT RESONANT FREQUENCY.

Transmitting side	Receiving side	CC	Output versus mutual inductance
S	S	Yes	Reverse Proportion
LCC	LCC	Yes	Proportion

For the fundamental harmonic component, the compensation network in Fig. 5(a) operates under an equivalent LCC-LCC topology, as analytically demonstrated in Fig. 5(b). The resonance relationship is shown in formula (10).

$$\begin{cases} j\omega_{\mathrm{s},1}L_{11} = -\dfrac{1}{j\omega_{\mathrm{s},1}C_{11}} = j\omega_{\mathrm{s},1}L_{\mathrm{P}} + \dfrac{1}{j\omega_{\mathrm{s},1}C_b} \\ j\omega_{\mathrm{s},1}L_{22} = -\dfrac{1}{j\omega_{\mathrm{s},1}C_{22}} = j\omega_{\mathrm{s},1}L_{\mathrm{S}} + \dfrac{1}{j\omega_{\mathrm{s},1}C_c} \end{cases}. \tag{10}$$

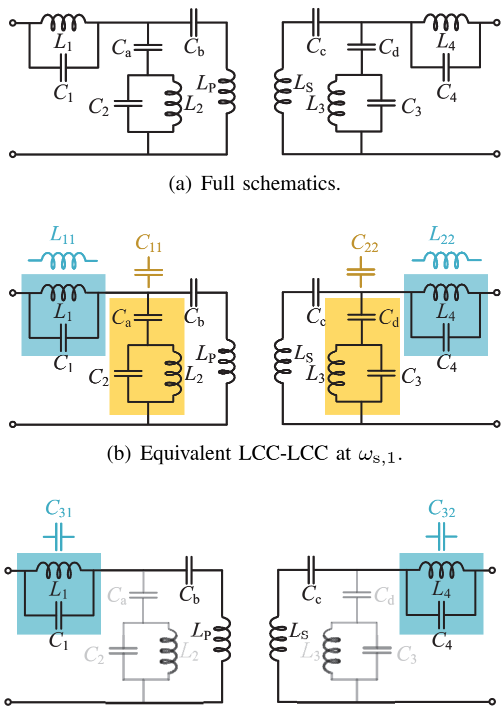

(a) Full schematics.

(b) Equivalent LCC-LCC at $\omega_{s,1}$.

(c) Equivalent S-S at $\omega_{s,2}$.

Fig. 5. Equivalent circuit.

where

$$\begin{cases} j\omega_{s,1}L_{11} = \dfrac{j\omega_{s,1}L_1\dfrac{1}{j\omega_{s,1}C_1}}{j\omega_{s,1}L_1+\dfrac{1}{j\omega_{s,1}C_1}} \\ \dfrac{1}{j\omega_{s,1}C_{11}} = \dfrac{1}{j\omega_{s,1}C_a} + \dfrac{j\omega_{s,1}L_2\dfrac{1}{j\omega_{s,1}C_2}}{j\omega_{s,1}L_2+\dfrac{1}{j\omega_{s,1}C_2}} \end{cases}, \tag{11}$$

and

$$\begin{cases} j\omega_{s,1}L_{22} = \dfrac{j\omega_{s,1}L_4\dfrac{1}{j\omega_{s,1}C_4}}{j\omega_{s,1}L_4+\dfrac{1}{j\omega_{s,1}C_4}} \\ \dfrac{1}{j\omega_{s,1}C_{22}} = \dfrac{1}{j\omega_{s,1}C_d} + \dfrac{j\omega_{s,1}L_3\dfrac{1}{j\omega_{s,1}C_3}}{j\omega_{s,1}L_3+\dfrac{1}{j\omega_{s,1}C_3}} \end{cases}. \tag{12}$$

Building on this theoretical foundation, existing studies for LCC-LCC compensated networks [34] theoretically demonstrate that the fundamental harmonic output current is mathematically formulated as:

$$I_{o,1} = |I_{o,1}| = \frac{MU_{L,1}}{j\omega_{s,1}L_{11}L_{22}}. \tag{13}$$

For the second harmonic, the compensation network of the circuit in Fig. 5(a) is equivalent to an S-S type, and its equivalent circuit is shown in Fig. 5(c). The resonance relationship is shown in formulas (14) and (15).

$$\begin{cases} \dfrac{1}{j\omega_{s,2}C_{31}} = -j\omega_{s,2}L_P - \dfrac{1}{j\omega_{s,2}C_b} = \dfrac{j\omega_{s,2}L_1\dfrac{1}{j\omega_{s,2}C_1}}{j\omega_{s,2}L_1+\dfrac{1}{j\omega_{s,2}C_1}} \\ j\omega_{s,2}L_2 + \dfrac{1}{j\omega_{s,2}C_2} = 0 \end{cases} \tag{14}$$

and

$$\begin{cases} \dfrac{1}{j\omega_{s,2}C_{32}} = -j\omega_{s,2}L_S - \dfrac{1}{j\omega_{s,2}C_c} = \dfrac{j\omega_{s,2}L_4\dfrac{1}{j\omega_{s,2}C_4}}{j\omega_{s,2}L_4+\dfrac{1}{j\omega_{s,2}C_4}} \\ j\omega_{s,2}L_3 + \dfrac{1}{j\omega_{s,2}C_3} = 0 \end{cases}. \tag{15}$$

Building on the above relationship, previous research on S-S compensation networks [35] indicates that the second harmonic component of the output current can be expressed as:

$$I_{o,2} = |I_{o,2}| = \frac{U_{L,2}}{j\omega_{s,2}M}. \tag{16}$$

The R_{eq} represents the AC equivalent resistance and can be expressed as:

$$R_{eq} = \frac{8R}{\pi^2}. \tag{17}$$

Ignoring the power loss of the rectifier bridge, based on the conservation of energy before and after the rectifier bridge, the following equation can be obtained:

$$\frac{I_{o,1}^2R_{eq}}{2} + \frac{I_{o,2}^2R_{eq}}{2} = I_{OUT}^2R. \tag{18}$$

The output current I_{OUT}, independent of the load, can be calculated using equations (13) and (16) as follows:

$$I_{OUT} = \frac{2}{\pi}\sqrt{(I_{o,1}^2+I_{o,2}^2)}. \tag{19}$$

B. Analysis of Misalignment Tolerance

According to formula (13), (16), and (19), the output current of the fundamental and second harmonic can be calculated as (20). For further discussion, this paper defines a parameter β, which further represents $I_{OUT,1}$ as β and other fixed parameters of the circuit.

$$\begin{cases} I_{OUT,1} = \dfrac{2U_{L,1}M}{\pi\omega_{s,1}L_{11}L_{22}} = \dfrac{2U_{L,1}M}{\beta\pi\omega_{s,1}L_PL_S} \propto \dfrac{M}{\beta}(0<\beta\le 1) \\ I_{OUT,2} = \dfrac{2U_{L,2}}{\pi\omega_{s,2}M} \propto \dfrac{1}{M} \end{cases}. \tag{20}$$

and

$$I_{OUT} = \sqrt{I_{OUT,1}^2 + I_{OUT,2}^2}. \tag{21}$$

Therefore, in the case where parameters other than mutual inductance M remain unchanged, I_{OUT} satisfies the following relationship

$$I_{\mathrm{OUT}} \propto \sqrt{\frac{1}{M^2} + \frac{M^2}{\beta^2}}. \tag{22}$$

As demonstrated by the objectives in Section II-A, the proposed circuit topology satisfies the fundamental design requirements. However, to optimize system performance across the specified misalignment range, the parameter β requires systematic investigation. We therefore formulate the output current relationship as $I_{\mathrm{OUT}}(M, \beta)$. Under aligned coil conditions (denoted by M_{N}), the output current is expressed by $I_{\mathrm{N}} = I_{\mathrm{OUT}}(M_{\mathrm{N}}, \beta)$. This study adopts the normalized current ratio $I_{\mathrm{OUT}}(M, \beta)/I_{\mathrm{N}}$ to quantify output current variations during misalignment.

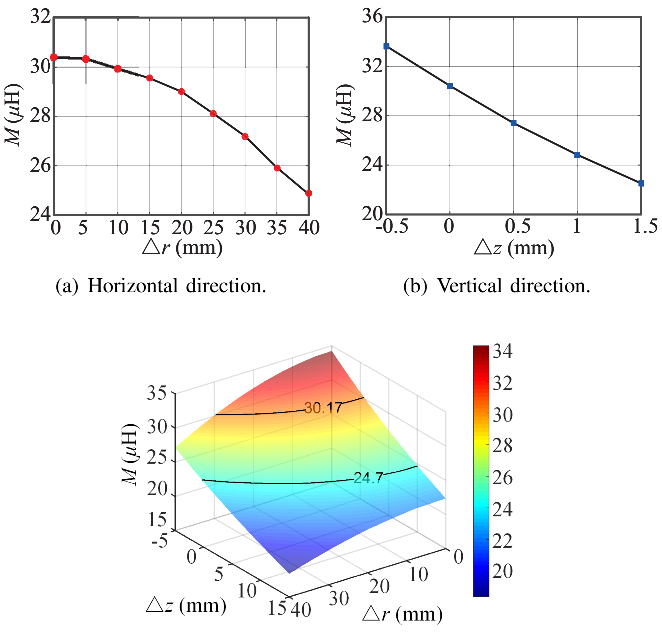

(a) Horizontal direction.

(b) Vertical direction.

(c) Horizontal and vertical directions.

Fig. 6. Mutual inductance versus misalignments.

To determine the appropriate value of parameter β, it is imperative to determine the variation range of M. The coil used in this paper is circular; Δr and Δz are used to indicate the misalignment distance in the horizontal and vertical directions, respectively. The variation in mutual inductance with misalignment is presented in Fig. 6. Based on this analysis, the misalignment tolerance of the circuit under different β values is illustrated in Fig. 7(a). In this paper, $\beta^2 = 0.2$ is selected. Fig. 7(b) demonstrates the output characteristics comparison between the proposed method and the conventional circuit, where $I_{\mathrm{OUT},1}$ and $I_{\mathrm{OUT},2}$ are used to represent the output characteristics of the conventional circuit as shown in (20). It is evident that the proposed method has lower output fluctuations within the range of mutual inductance variation studied. In addition, the above analysis shows that the proposed misalignment tolerance improvement method is load-independent, which means that the proposed method can improve the misalignment tolerance in a wide load range.

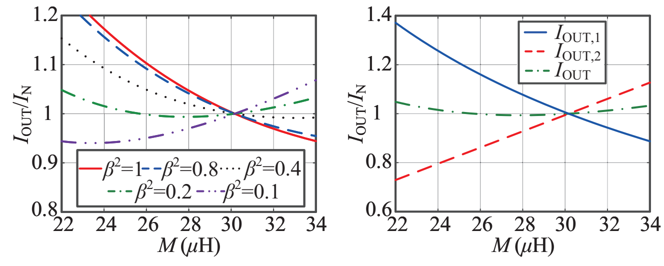

(a) Output current versus different β

(b) Comparison

Fig. 7. Output current variations versus M.

C. Parameters Design and Analysis

In the proposed method, the values of inductors L_{AC}, L_2, and L_3 in Fig. 2 have degrees of design freedom, so they have room for optimization. The optimization process necessitates the use of circuit simulation software. Using L_{AC} as an example, as illustrated in Fig. 8, for any given value of L_{AC}, the ZVS margin D_{Z} can be tuned to achieve the target value by adjusting C_{E}, while the root mean square (RMS) current through L_{AC} is simultaneously obtained and recorded in Fig. 9. As the inductance of L_{AC} increases, the rate at which the decrease of the current I_L slows down. Therefore, it is advisable to select a point where the current in L_{AC} starts varying slowly. This choice helps reduce both the cost and power losses of the converter. In this paper, the inductance L_{AC} is chosen as 44 μH, and the corresponding value of C_{E} is determined to be 21.5 nF, which can be determined correspondingly. Similarly, the values of inductance L_2 and L_3 can be determined by the same method.

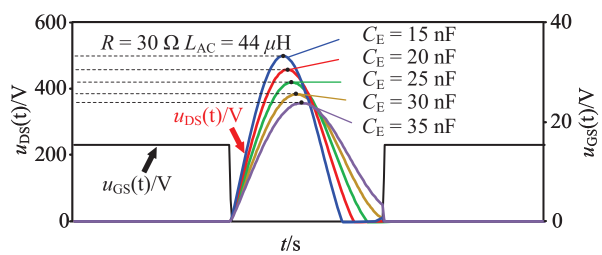

Fig. 8. The ZVS condition versus the value of C_{E}.

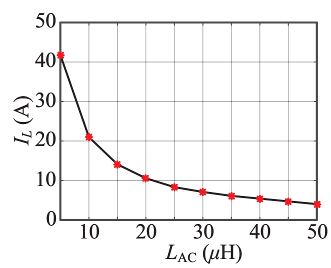

Fig. 9. Relationship between I_L and L_{AC}.

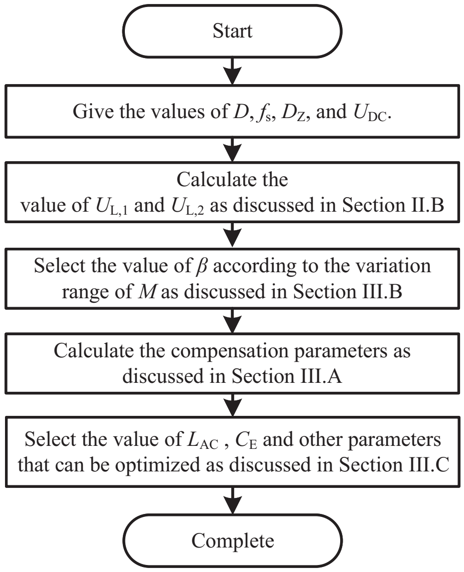

Fig. 10. The parameter design process of the proposed circuit.

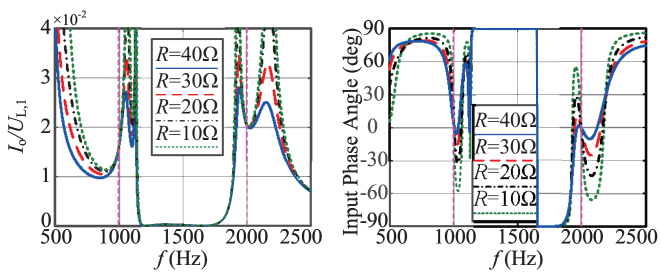

(a) Transfer gain (b) Input phase angle

Fig. 11. Characteristics of proposed single-ended IPT circuit.

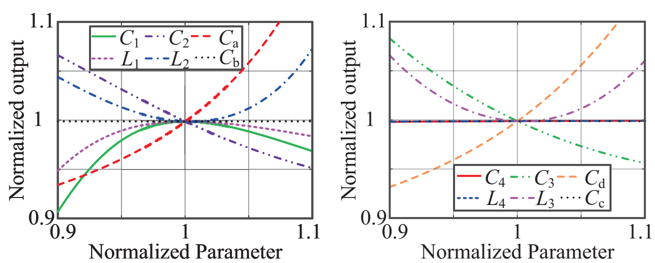

(a) Primary side (b) Secondary side

Fig. 12. Normalized output with varying normalized parameters.

Based on the above analysis, parameter design and calculation can be carried out for the proposed circuit as shown in Fig. 10, with detailed parameters shown in Table IV. Using the circuit parameters in Table IV, a characteristic analysis of the proposed circuit is conducted. Fig. 11(a) illustrates the transfer gain of the circuit as a function of switching frequency, with different curves representing various load conditions. The curves clearly intersect at 100 kHz and 200 kHz, indicating that the proposed circuit exhibits two load-independent resonance points. Fig. 11(b) shows the impedance angle of the proposed circuit's input impedance as a function

TABLE IV
PARAMETERS OF PROPOSED CIRCUIT

Symbol	Definition	Value
C_E	Transmitting-side compensation capacitor	21.5 nF
C_1	Transmitting-side compensation capacitor	30.71 μF
C_2	Transmitting-side compensation capacitor	12.67 nF
C_a	Transmitting-side compensation capacitor	22.17 nF
C_b	Transmitting-side compensation capacitor	108.18 nF
C_c	Receiving-side compensation capacitor	106.76 nF
C_d	Receiving-side compensation capacitor	22.17 nF
C_3	Receiving-side compensation capacitor	12.67 nF
C_4	Receiving-side compensation capacitor	30.19 nF
L_{AC}	Transmitting-side compensation inductor	44 μH
L_1	Transmitting-side compensation inductor	30.18 μH
L_2	Transmitting-side compensation inductor	50.12 μH
L_3	Receiving-side compensation inductor	50.09 μH
L_4	Receiving-side compensation inductor	30.66 μH
L_P	The inductance of the transmitting coil	71.03 μH
L_S	The inductance of receiving coil	71.31 μH
M	Mutual inductance	30.17 μH
f_s	Operating frequency	100 kHz
$U_{L,1}$	Calculated amplitude of fundamental harmonic	177.26 V
$U_{L,2}$	Calculated amplitude of second harmonic	121.42 V
U_{DC}	Input DC voltage	100 V
I_{OUT}	Output DC current	2.4 A
D	Duty cycle	0.5
D_Z	ZVS margin	0.11

of switching frequency. At operating frequencies of 100 kHz and 200 kHz, the phase angle of the input impedance is 0 degrees, regardless of the load value.

The sensitivity analysis of the compensation parameters is presented in Fig. 12. It can be observed that parameters C_a and C_d exhibit higher sensitivity compared to the others, thus requiring greater accuracy in their selection. In contrast, the sensitivity curves of parameters C_4, L_4, C_b, and C_c almost coincided, and showed very low sensitivity.

IV. Experimental Validation

To validate the analysis, a 172.8 W single-ended IPT prototype has been constructed, as illustrated in Fig. 13. This prototype includes a DC input, a transmitting circuit, a magnetic coupler, a receiving circuit, an oscilloscope, and an electronic load, labeled as components 1 through 6. The magnetic coupler employs two coaxial circular coils with a diameter of 22.8 cm, serving as the transmitter and receiver, respectively. These components are separated by an axial gap of 5 cm. Both coils are fabricated from 3 mm diameter Litz wire, wound into 16 turns per coil, and encased in ferrite shielding to enhance magnetic flux concentration. Additional structural and dimensional specifications are illustrated in Fig. 13. The MOSFET used is a CGE1M120080, and the receiving-side rectifier circuit comprises four MBR20200 diodes. The electronic load is used to simulate the equivalent load.

A. ZVS Condition

Figs. 14(a) and (b) illustrate the soft-switching waveforms at different operating conditions. At an operating frequency of 100 kHz and a 50% duty cycle, the measured amplitudes of $U_{DS}(t)$ are 455 V for aligned and 459 V for misalignment. The ZVS margin remains nearly constant despite variations in the misalignment.

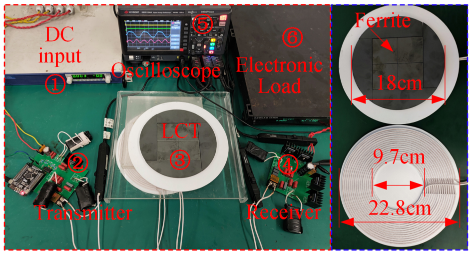

Fig. 13. Photograph of the proposed dual-frequency single-ended IPT converter.

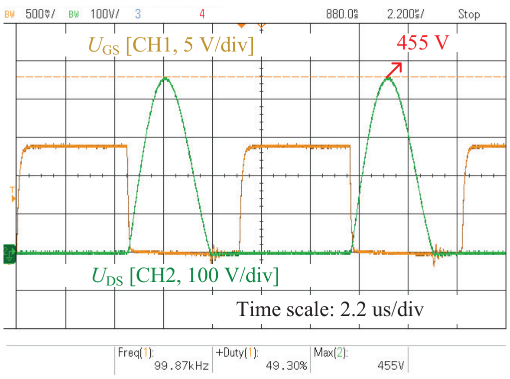

(a) Waveforms of ZVS (aligned).

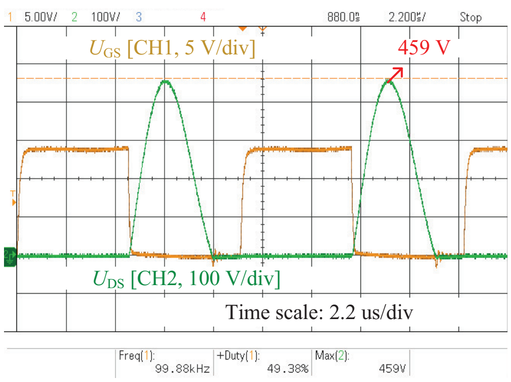

(b) Waveforms of ZVS ($\Delta r = 40mm$ or $\Delta z = 10mm$).

Fig. 14. Waveforms of ZVS.

B. Misalignment Tolerance

Fig. 15 illustrates the current waveforms of the proposed circuit under both aligned and maximum misalignment conditions of the coils when $R = 30\ \Omega$. As clearly demonstrated in Fig. 15(a), when the coils are properly aligned, the output voltage (U_O) measures 72.305 V and the output current (I_O) measures 2.3933 A, the RMS value of the transmitting coil current (i_P) measures 4.188 A, while that of the receiving coil current (i_S) is 2.438 A. In contrast, the corresponding output voltage and current values presented in Fig. 15(b) under maximum misalignment condition are 72.332 V and 2.609 A. And the coil currents are 4.358 A and 2.502 A for the transmitting and receiving coils, respectively. Furthermore, Fig. 16 displays the waveforms of output voltage, output current, and coil currents when the load is 30 Ω and the displacement Δr is continuously varied from 0 mm to 40 mm. Notably, during the entire displacement process, both U_O and I_O remain virtually constant. Fig. 17 and Fig. 18 illustrate the corresponding waveforms under a light load ($R = 7.5\ \Omega$). Comparative analysis of the output voltage and current (U_O and I_O) characteristics between these two scenarios reveals that the occurrence of coil misalignment does not exhibit a significant impact on the operational performance of the proposed circuit.

Fig. 19 characterizes the output current variation with respect to displacement. At maximum displacement (Δr=40 mm), the output current slightly exceeds the rated output level, which aligns with the theoretical design illustrated in Fig. 7.

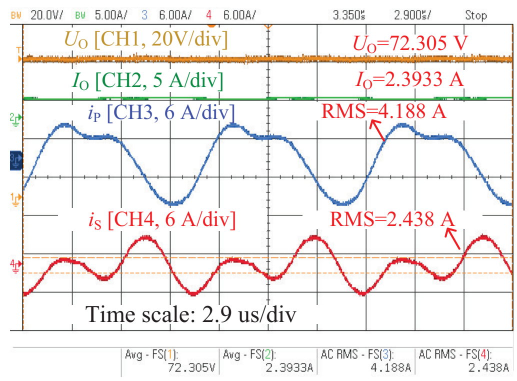

(a) U_O, I_O, i_P, and i_S (aligned).

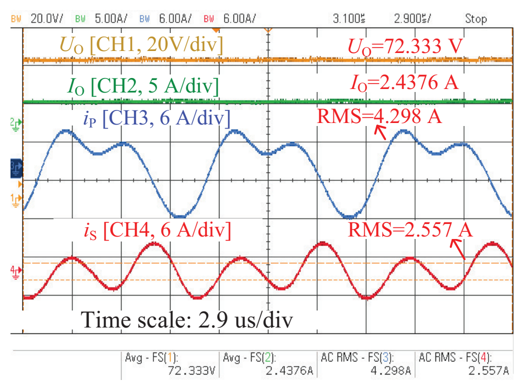

(b) U_O, I_O, i_P, and i_S ($\Delta r = 40\ mm$ or $\Delta z = 10\ mm$).

Fig. 15. Voltage and current waveforms when $R = 30\ \Omega$.

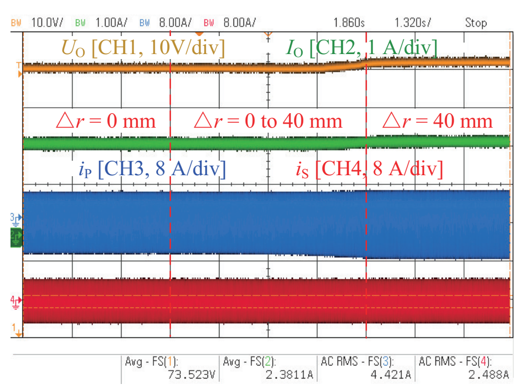

Fig. 16. Coil currents and output waveforms versus Δr when $R = 30\ \Omega$.

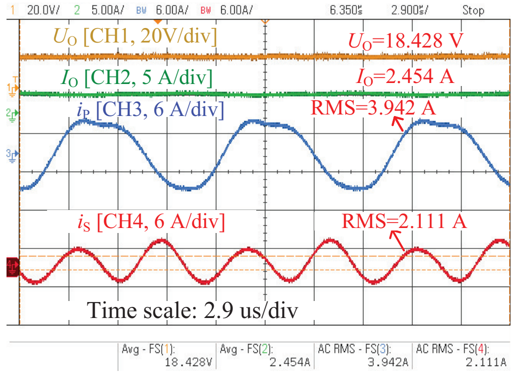

(a) $U_{\rm O}$, $I_{\rm O}$, $i_{\rm P}$, and $i_{\rm S}$ (aligned).

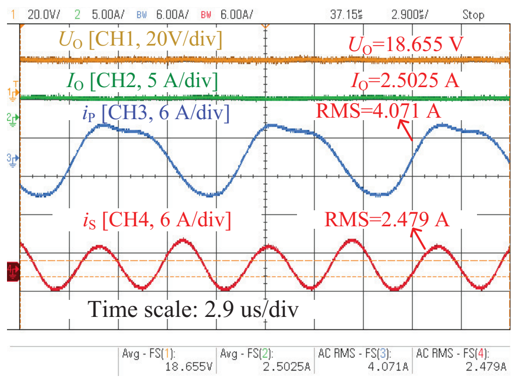

(b) $U_{\rm O}$, $I_{\rm O}$, $i_{\rm P}$, and $i_{\rm S}$ ($\Delta r = 40mm$ or $\Delta z = 10\ mm$).

Fig. 17. Voltage and current waveforms when $R = 7.5\ \Omega$.

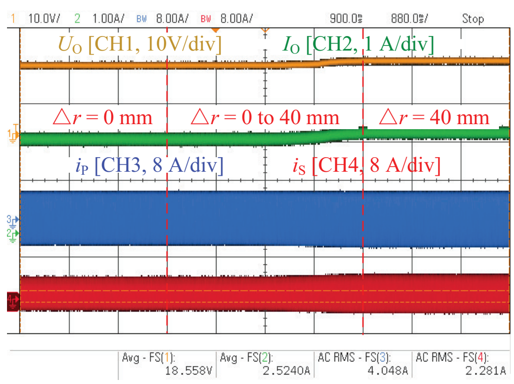

Fig. 18. Coil currents and output waveforms versus Δr when $R = 7.5\ \Omega$.

C. Load-independent Output

Fig. 20 presents the load switching experiments of the proposed circuit with the coil currents as the reference waveforms under both aligned and maximum misalignment conditions. Notably, in both operational scenarios, when the load changes from 3 Ω to 30 Ω, the output current ($I_{\rm O}$) of the proposed circuit remains virtually constant. Furthermore, Fig. 21 shows the output current versus load condition in the case of aligned and maximum misalignment. The load range is 3-30 Ω. The experimental evidence demonstrates conclusively that the proposed methodology ensures approximately load-independent characteristics of the output current, regardless of whether coil misalignment occurs in the system. The experimental

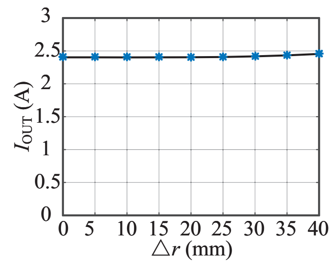

(a) $R = 30\ \Omega$

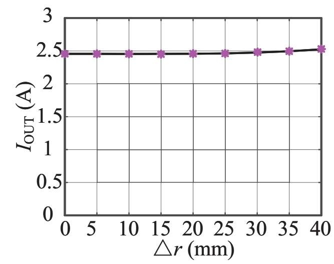

(b) $R = 7.5\ \Omega$

Fig. 19. Output current versus Δr.

verification in Section IV.C and Section IV.D shows that the proposed method can improve the misalignment tolerance in a wide load range.

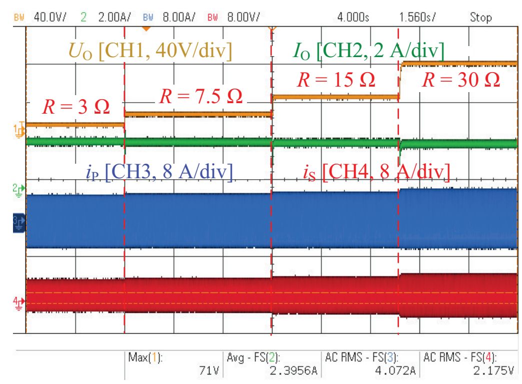

(a) $U_{\rm O}$, $I_{\rm O}$, $i_{\rm P}$, and $i_{\rm S}$ (aligned).

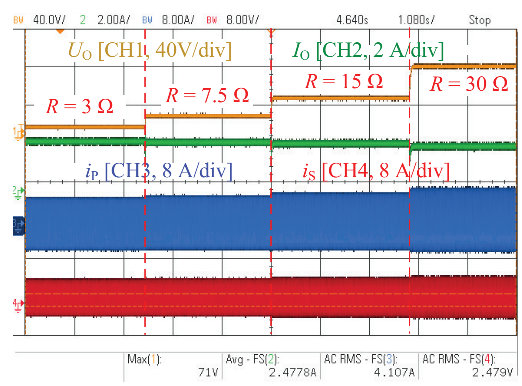

(b) $U_{\rm O}$, $I_{\rm O}$, $i_{\rm P}$, and $i_{\rm S}$ ($\Delta r = 40\ mm$ or $\Delta z = 10\ mm$).

Fig. 20. Output and coils currents waveforms when the load switches.

D. Efficiency

Fig. 22(a) quantifies the DC-to-DC conversion efficiency under various misalignment conditions. With a 30 Ω load, the system efficiency reaches approximately 90.07% under alignment and maintains above 85% even at maximum displacement (Δr=40 mm).

To elucidate the cause of efficiency degradation, Fig. 22(b) illustrates the power loss distribution of the system under both aligned and maximum misaligned conditions. Here, $P_{\rm loss,a}$ and

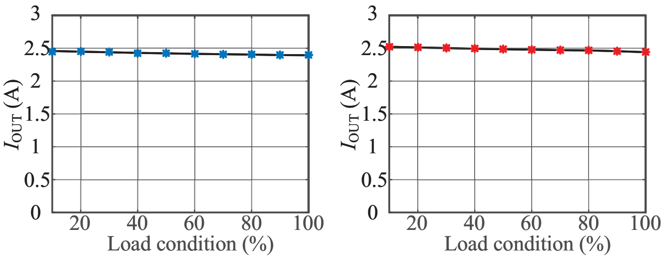

(a) Output current (aligned).

(b) Output current ($\Delta r = 40\ mm$ or $\Delta z = 10\ mm$).

Fig. 21. Output current versus load condition.

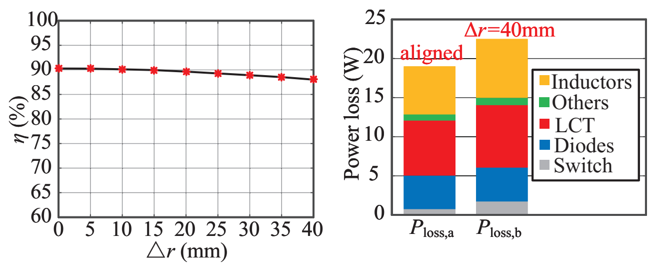

(a) Efficiency

(b) Power losses.

Fig. 22. Efficiency and power losses when $R = 30\ \Omega$.

$P_{\mathrm{loss,b}}$ denote the power losses under alignment and maximum misalignment, respectively. Specifically, as the coupling coefficient decreases, the operating principle of the proposed method leads to an increase in the current through the coil and inductor to compensate for the output variation induced by misalignment, thereby resulting in corresponding power losses. Furthermore, misalignment results in higher switch conduction current, thereby increasing the conduction loss of the switch.

V. Conclusion

To enhance omnidirectional misalignment tolerance across a wide load range and avoid increasing the complexity of the magnetic couplers and control circuits, this paper proposes a dual-band complementary compensation for a 2-coil single-ended IPT converter. Based on the high second harmonic content in a single-ended IPT inverter, the proposed method establishes power transfer channels for the second harmonic generated by the inverter, while simultaneously utilizing it to counteract output fluctuations caused by misalignment conditions. A prototype with a 2.4 A load-independent output current and 172.8 W output power has been developed. Experimental results demonstrate that the circuit enhances omnidirectional misalignment tolerance across a wide load range and maintains a load-independent output within different operating conditions. And the proposed method maintains stable output current within the investigated misalignment range while achieving a transfer efficiency exceeding 85%. Moreover, compared with other dual-frequency resonant methods, the proposed method is independent of the design of the magnetic coupler and exhibits universal applicability to 2-coil magnetic couplers with arbitrary parameters.

References

[1] C. Liu, X. Gao, and S. Cui, "A dual-layer receiver with low interlayer voltage stress and high power density for EVs wireless charging system," *IEEE Trans. Ind. Electron.,* vol. 72, no. 4, pp. 3551–3561, Apr. 2025.

[2] Y. Gong, Z. Zhang, and S. Chang, "Single-transmitter-controlled multiple-channel constant current outputs for in-flight wireless charging of drones," *IEEE Trans. Ind. Electron.,* vol. 71, no. 4, pp. 3606–3616, Apr. 2024.

[3] T. Feng, K. Shi, J. Jiang, and P. Wang, "A solenoid magnetic coupler and its control method for omnidirectional wireless charging of UAVs," *IEEE Trans. Ind. Electron.,* vol. 72, no. 3, pp. 2540–2550, Mar. 2025.

[4] J. Lee, B. Bae, B. Kim, J. Lim, and B. Lee, "A load-independent battery charging system for multiple wearable devices using conductive textile," *IEEE Trans. Ind. Electron.,* vol. 71, no. 11, pp. 15211–15215, Nov. 2024.

[5] H. Luo, Z. Wei, C. Wang, X. Tan, and H. Li, "Single-switch cordless kitchen appliances: segmented duty cycle control for ZVS and energy injection-based MOD," *IEEE Trans. Ind. Electron.,*Accepted, doi: 10.1109/TIE.2025.3581193.

[6] H. Zhang, C. K. Lee, and Z. Li, "Six degrees of freedom tracking and wireless charging for capsule endoscopy," *IEEE Trans. Ind. Electron.,* vol. 72, no. 4, pp. 3643–3652, Apr. 2025.

[7] H. Zhang, W. Liu, Z. Li, and C. K. Lee, "Pulse frequency modulation of 3D wireless power transfer for capsule endoscopy," *IEEE Trans. Ind. Electron.,* vol. 72, no. 1, pp. 308–317, Jan. 2025.

[8] H. Zhou, Z. Shen, Y. Wu, X. Chen, and Y. Zhang, "A stable dynamic electric vehicle wireless charging system based on triple decoupling receiving coils and a novel triple-diode rectifier," *IEEE Trans. Ind. Electron.,* vol. 71, no. 10, pp. 12011–12018, Oct. 2024.

[9] Y. Zhang, C. Liu, M. Zhou, and X. Mao, "A novel asymmetrical quadrupolar coil for interoperability of unipolar, bipolar, and quadrupolar coils in electric vehicle wireless charging systems," *IEEE Trans. Ind. Electron.,* vol. 71, no. 4, pp. 4300–4303, Apr. 2024.

[10] B. Zou, Z. Huang, I. W. Iam, and C. S. Lam, "Tuning control against coupler parameter variations due to misalignment in an optimal-efficiency-tracking and constant-power-output IPT system," *IEEE Trans. Ind. Electron.,* vol. 40, no. 5, pp. 7500–7511, May 2025.

[11] A. Berger, M. Agostinelli, S. Vesti, J. A. Oliver, J. A. Cobos, and M. Huemer, "A wireless charging system applying phase-shift and amplitude control to maximize efficiency and extractable power," *IEEE Trans. Power Electron.,* vol. 30, no. 11, pp. 6338–6348, Nov. 2015.

[12] Y. Jiang, L. Wang, Y. Wang, J. Liu, X. Li, and G. Ning, "Analysis, design, and implementation of accurate ZVS angle control for EV battery charging in wireless high-power transfer," *IEEE Trans. on Ind. Electron.,* vol. 66, no. 5, pp. 4075–4085, May 2019.

[13] T. Mishima and C. M. Lai, "Zero-phase-angle load-independent and adaptable dual-side LCC inductive wireless power transfer system,"*IEEE Trans. Transp. Electrif.,* vol. 10, no. 2, pp. 3492–3503, Jun. 2024.

[14] Z. Hua, K. T. Chau, W. Liu, X. Tian, and H. Pang, "Autonomous pulse frequency modulation for wireless battery charging with zero-voltage switching," *IEEE Trans. on Ind. Electron.,* vol. 70, no. 9, pp. 8959–8969, Sep. 2023.

[15] B. Zou and Z. Huang, "Primary-frequency-tuning and secondary-impedance-matching IPT converter with programmable constant power output and optimal efficiency tracking against variation of coupling coefficient," *IEEE Trans. Power Electron.,* vol. 39, no. 4, pp. 4895–4909, Apr. 2024.

[16] H. Xu, Z. Huang, X. L. Li, and C. K. Tse, "Misalignment-tolerant IPT coupler with enhanced magnetic flux variation suppression and reduced copper usage," *IEEE Trans. Power Electron.,* vol. 39, no. 8, pp. 10506–10517, Aug. 2024.

[17] H. Xu and Z. Huang, "Alternately arranged segmented transmitter pads with magnetic field complementation for suppressing power fluctuation in dynamic wireless power transfer," *IEEE Trans. Power Electron.,* vol. 39, no. 10, pp. 14091–14102, Oct. 2024.

[18] X. Duan, W. Han, Y. Hu, H. Tian, and J. Huang, "2-D misalignment-tolerant wireless power transfer with a compact O-to-OXY magnetic coupler," *IEEE J. Emerg. Sel. Topics Ind. Electron.,* vol. 6, no. 1, pp. 9–18, Jan. 2025.

[19] Z. Shen, H. Zhou, R. Xie, Y. Zhuang, X. Mao, and Y. Zhang, "A strong offset-resistant electric vehicle wireless charging system based on dual decoupled receiving coils," *IEEE Trans. on Ind. Electron.,* vol. 71, no. 11, pp. 15216–15219, Nov. 2024

[20] X. Qu, Y. Yao, D. Wang, S. C. Wong, and C. K. Tse, "A family of hybrid IPT topologies with near load-independent output and high tolerance to pad misalignment," *IEEE Trans. Power Electron.,* vol. 35, no. 7, pp. 6867–6877, Jul. 2020.

[21] G. Ke, Q. Chen, S. Zhang, X. Xu, and L. Xu, "A single-ended hybrid resonant converter with high misalignment tolerance," *IEEE Trans. Power Electron.,* vol. 37, no. 10, pp. 12841–12852, Oct. 2022.
[22] G. Ke, Q. Chen, L. Xu, X. Ren, and Z. Zhang, "Analysis and optimization of a double-sided S-LCC hybrid converter for high misalignment tolerance," *IEEE Trans. on Ind. Electron.,* vol. 68, no. 6, pp. 4870–4881, Jun. 2021.
[23] P. Zhao, J. Liang, H. Wang, and M. Fu, "Detuned LCC/S-S compensation for stable-output inductive power transfer system under ultrawide coupling variation," *IEEE Trans. on Ind. Electron.,* vol. 38, no. 10, pp. 12342–12347, Oct. 2023.
[24] C. Chen, C. Q. Jiang, T. Ma, X. Wang, Y. Fan and J. Xiang, "Misalignment tolerance extension for inductive power transfer system by utilizing slight frequency-detuned compensation,"*IEEE Trans. Transp. Electrif.,* vol. 10, no. 4, pp. 9748–9760, Dec. 2024,
[25] W. Liu, K. T. Chau, C. H. T. Lee, W. Han, X. Tian, and W. H. Lam, "Full-range soft-switching pulse frequency modulated wireless power transfer," *IEEE Trans. Power Electron.,* vol. 35, no. 6, pp. 6533–6547, Jun. 2020.
[26] C. Jiang, K. T. Chau, W. Liu, C. Liu, W. Han, and W. H. Lam, "An LCC-compensated multiple-frequency wireless motor system," *IEEE Trans. on Ind. Inform.,* vol. 15, no. 11, pp. 6023–6034, Nov. 2019.
[27] W. Zhong and S. Y. R. Hui, "Maximum energy efficiency operation of series-series resonant wireless power transfer systems using On-Off keying modulation," *IEEE Trans. Power Electron.,* vol. 33, no. 4, pp. 3595–3603, Apr. 2018.
[28] W. Xiong, Q. Yu, and Z. Liu, "A dual-frequency-detuning method for improving the coupling tolerance of wireless power transfer," *IEEE Trans. Power Electron.,* vol. 38, no. 6, pp. 6923–6928, Jun. 2023.
[29] Z. Liu, M. Su, Q. Zhu, L. Zhao, and A. P. Hu, "A dual frequency tuning method for improved coupling tolerance of wireless power transfer system," *IEEE Trans. Power Electron.,* vol. 36, no. 7, pp. 7360–7365, Jul. 2021.
[30] Z. Dai and J. Wang, "A dual-frequency WPT Based on multilayer self-decoupled compact coil and dual CLCL hybrid compensation topology," *IEEE Trans. Power Electron.,* vol. 37, no. 11, pp. 13955–13965, Nov. 2022.
[31] J. Wang, Z. Huang, and X. L. Li, "A dual-frequency resonant single-ended IPT converter with enhanced power transfer capability," *IEEE Trans. Ind. Electron.,* vol. 72, no. 8, pp. 7964–7973, Aug. 2025
[32] Z. Guo, C. Wang, S. Lin, L. Yang, and X. Lu, "Multiparallel and flexible expansion of single-switch WPT inverter by magnetic integration," *IEEE Trans. Power Electron.,* vol. 38, no. 3, pp. 4167–4180, Mar. 2023.
[33] J. Wang and Z. Huang, "A single-switch WPT circuit with inherent CCO-CVO for battery charging,"*IEEE Trans. Transp. Electrif.,* vol. 10, no. 1, pp. 1957–1968, Mar. 2024.
[34] Y. Chen, H. Zhang, C. S. Shin, C. H. Jo, S. J. Park and D. H. Kim, "An efficiency optimization-based asymmetric tuning method of double-sided LCC compensated WPT system for electric vehicles," *IEEE Trans. Power Electron.,* vol. 35, no. 11, pp. 11475–11487, Nov. 2020.
[35] J. Liu, K. W. Chan, C. Y. Chung, N. H. L. Chan, M. Liu, and W. Xu, "Single-stage wireless-power-transfer resonant converter with boost bridgeless power-factor-correction rectifier," *IEEE Trans. on Ind. Electron.,* vol. 65, no. 3, pp. 2145–2155, Mar. 2018.

Jingyu Wang was born in Tai'an, China, in 1996. He received a B.S. degree in electrical engineering and automation from Hefei University of Technology, Hefei, China, in 2019 and an M.S. degree in electrical engineering from Qingdao University, Qingdao, China, in 2022. He is currently working toward a Ph.D. degree in the Shien-Ming Wu School of Intelligent Engineering, South China University of Technology, Guangzhou, China.

His current research interests mainly include wireless power transfer.

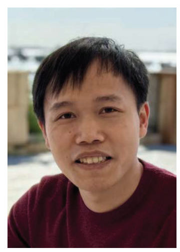

Zhicong Huang (Senior Member, IEEE) received the B.Eng. degree in electrical engineering and automation and the M.Eng. degree in mechanical and electronic engineering from Huazhong University of Science and Technology, Wuhan, China, in 2010 and 2013, respectively, and the Ph.D. degree in power electronics from The Hong Kong Polytechnic University, Hong Kong, China, in 2018.

Since 2020, he has been an Associate Professor with Shien-Ming Wu School of Intelligent Engineering, South China University of Technology, Guangzhou, China. In 2019, he was a Postdoctoral Fellow under the UM Macao Talent Program with the State Key Laboratory of Analog and Mixed-Signal VLSI, Macau, China. His research interests include wireless power transfer, resonant power conversion, large-scale renewable power generation, artificial intelligence for power electronics, and wave energy converters.

Dr. Huang received the Outstanding Reviewer Award for IEEE TRANSACTIONS ON POWER ELECTRONICS in 2024 and 2021, the Star Reviewer Award for IEEE JOURNAL OF EMERGING AND SELECTED TOPICS IN POWER ELECTRONICS in 2024 and 2023, and the Best Reviewer for IEEE JOURNAL ON EMERGING AND SELECTED TOPICS IN CIRCUITS AND SYSTEMS in 2023. He serves as an Associate Editor of IEEE TRANSACTIONS ON CONSUMER ELECTRONICS.